NASA TECHNICAL MEMORANDUM

NASA TM-73839

NASA TM-73839

FAR-FIELD MULTIMODAL ACOUSTIC RADIATION DIRECTIVITY

by Arthur V. Saule and Edward J. Rice
Lewis Research Center
Cleveland, Ohio 44135

TECHNICAL PAPER to be presented at the
Ninety-fourth Meeting of the
Acoustical Society of America
Miami Beach, Florida, December 12-16, 1977

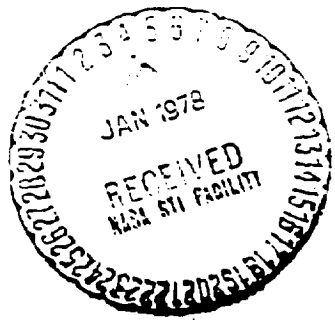

FAR-FIELD MULTIMODAL ACOUSTIC RADIATION DIRECTIVITY

by Arthur V. Saule and Edward J. Rice

Lewis Research Center

ABSTRACT

Approximate equations for the far-field acoustic radiation patterns in the forward quadrant from a flanged circular duct, recently presented by Rice, were compared with exact equations for both single and multimodal excitations. The single mode comparison showed good agreement between the exact and approximate equations for the principal lobes of higher radial order modes. For lower and especially for zero radial order modes, there was some error in the angular location and decibel level of principal lobe peak pressure obtained from the approximate equation. Some agreement of sidelobes was also observed although the approximate equation was not intended to simulate the sidelobes. The multimodal approximate summation equations consisting only of a simple function of directivity angle and an acoustic power biasing function were checked against the exact equations for several distributions of modal power. The results showed an excellent agreement with exact equations for all cases. A check about significant modal participation in a multimodal pattern showed that many modes contribute to the final level and shape of the directivity curve but the major contributions appear to come from the higher radial order modes.

E-9426

INTRODUCTION

Information about the structure of propagating acoustic duct modes produced by turbofan engines is essential to the design of acoustic suppressors in engine ducts. The modal structure can be determined directly from in-duct acoustic pressure measurements. This approach has been successfully applied for quite simple modal structures (Ref. 1); however, it may require sophisticated measurement and analysis techniques to account for all participating modes. The internal modal structure also can be obtained from far-field directivity patterns. An analysis of measured far-field acoustic radiation patterns may provide a relatively simple way of identifying a modal structure that is adequate for liner design.

The far-field acoustic radiation patterns produced by a single circular duct mode and their directional characteristics have been theoretically studied in the past for flanged ducts (Refs. 2 to 4), as well as for unflanged ducts (Refs. 4 and 5). Lately, multimodal radiation patterns representing summations of many duct modes also have attracted some interest (Ref. 6). The calculations required for a single mode as well as for multimodal summation are relatively straightforward but are usually time consuming. Simplifying assumptions, however, can be made by which approximate directivity patterns can be readily defined and evaluated.

Approximate equations for the far-field acoustic radiation patterns in the forward quadrant from a flanged circular duct were recently presented by Rice (Ref. 7) for both single mode and multimodal excitations. In Ref. 7, the single mode radiation equations for equal acoustic power per mode (Ref. 6) were simplified, and the multimodal summation equations were made independent of the number of participating modes. Thus, the approximate equations appear to have considerable future potential in performing far-field acoustic calculations. The approximate equations also make it possible to treat cases other than equal acoustic power per mode by use of an acoustic power biasing function. However, a wider acceptance and utility of the approximate equations rests on the demonstration of the range of their validity and accuracy.

As indicated in Ref. 7, the single mode approximate equations were introduced for the purpose of developing a method to determine the acoustic power produced by multimodal sources. A cautioning note about the shortcomings of the single mode approximate equations was also added in the reference. In the present paper, several single mode radiation patterns calculated from the exact equation (Ref. 6) are compared to the patterns obtained from the approximate equation (Ref. 7) to determine in more detail the range of validity of the approximate approach. The single mode comparisons are made for three categories of modes: (1) modes with varying radial order, but with constant circumferential order and source frequency, (2) modes with varying circumferential order, but with constant radial order and source frequency, and (3) the last cut-on modes with constant circumferential order, but with varying radial order and source frequency.

Observations were made in Ref. 7 that modes with similar cut-off ratios will produce similar directivity patterns and that the principal lobes are also dominant in multimodal radiation patterns. These observations lead to development of simplified summation equations. Sets of relatively closely spaced groups of principal lobes from exact radiation patterns at three directivity angles are examined in the present paper to check the assumptions arising from the above observations.

The multimodal approximate summation equation consisting only of a simple function of directivity angle and an acoustic power biasing function was checked in Ref. 7 for the equal acoustic power per mode case. In this paper, exact calculations were made for two cases of unequal power per mode, in addition to equal acoustic power per mode, to test the validity of the approximate multimodal summation equations over the entire range of forward quadrant directivity angles. Finally, modal participation in the directivity patterns of multimodal summations is examined, and a comparison with a directivity typical of experimental data is made.

SYMBOL LIST

c speed of sound, m/sec

D duct diameter, m

f source frequency, Hz

J'_m derivative of Bessel function of first kind and order m with respect to its argument

m circumferential order of an acoustic mode (also order of Bessel function)

n exponent of acoustic power biasing function, see Eq. (25)

p^2 far-field nondimensional total mean-square pressure of all participating modes, see Eq. (22)

$p^2_{m,\mu}$ far-field nondimensional mean-square pressure of a single mode, Eq. (1)

$(P_p)^2_{m,\mu}$ far-field mean-square pressure of principal lobe peak, see Eq. (11)

s total number of sidelobes in a directivity pattern, see Eq. (21)

s_a number of aft sidelobes in a directivity pattern, see Eq. (20)

s_f number of forward sidelobes in a directivity pattern, see Eq. (17)

z_0 position function of a node or lobe terminal, see Eq. (15)

$z^*_{m,\mu}$ exact position function of principal lobe peak pressure, see Eq. (8)

$\alpha_{m,\mu}$ hardwall duct mode eigenvalue, see Eq. (4)

$\beta_{m,\mu}$ acoustic power biasing function, see Eq. (25)

η frequency parameter, see Eq. (2)

μ radial order of an acoustic mode

$\xi_{m,\mu}$ mode cut-off ratio, see Eq. (3)

ψ far-field directivity angle measured from inlet duct center line, deg

ψ_0 far-field directivity angle of a node, deg, see Eq. (13)

$(\psi_p)_{m,\mu}$ far-field directivity angle of principal lobe peak pressure, deg, see Eq. (9)

Primed symbols denote derivatives with respect to the argument.

DIRECTIVITY EQUATIONS

In Ref. 7, a number of approximate equations for far-field acoustic radiation patterns in the forward quadrant from a flanged circular duct were presented for both single mode and multimodal excitations. In this section, the

so-called exact and approximate equations of interest are presented. They will be used in later sections to calculate the far-field directivity patterns and to check the validity of the approximate approach.

Single Mode Equations

A single mode far-field mean-square pressure acoustic radiation expression for a flanged circular duct for equal acoustic power per mode was derived in Ref. 6 and modified in Ref. 7 as follows:

$$P^2_{m,\mu}(\psi) = \frac{\sin^2\psi \; J'^2_m(\pi\eta \sin\psi)\sqrt{1 - (1/\xi_{m,\mu})^2}}{\left[1 - (m/\alpha_{m,\mu})^2\right]\left[(1/\xi_{m,\mu})^2 - \sin^2\psi\right]^2} \tag{1}$$

where the frequency parameter η is defined as

$$\eta = \frac{fD}{C} \tag{2}$$

and the mode cut-off ratio $\xi_{m,\mu}$ is defined as

$$\xi_{m,\mu} = \frac{\pi\eta}{\alpha_{m,\mu}} \tag{3}$$

The mode eigenvalue $\alpha_{m,\mu}$ is determined from the following equation:

$$J'_m(\alpha_{m,\mu}) = 0 \tag{4}$$

Equation (1) will be referred to here as an exact single mode equation. It was derived for zero axial Mach number, negligible end reflections, and the constant has been omitted. The equation is expressed in the notation of Ref. 7, except for the modal subscripts m,μ which are added here to emphasize the single mode relations.

In Ref. 7, the following approximate single mode acoustic radiation expression was derived from Eq. (1):

$$P^2_{m,\mu}(\psi) \approx \frac{2 \sin\psi \sin^2\left[\pi\eta(\sin\psi - 1/\xi_{m,\mu})\right]\sqrt{1 - (1/\xi_{m,\mu})^2}}{\pi^2\eta\left[(1/\xi_{m,\mu})^2 - \sin^2\psi\right]^2} \tag{5}$$

Equation (5) will be referred to here as an approximate single mode equation. It was derived from Eq. (1) by using the following assumptions:

$$(m/\alpha_{m,\mu})^2 \ll 1 \tag{6}$$

and

$$J'(\pi\eta \sin\psi) \approx -\sqrt{\frac{2}{\pi^2\eta \sin\psi}} \sin(\pi\eta \sin\psi - \alpha_{m,\mu}) \tag{7}$$

The sinusoidal approximation to the Bessel function is known to be most accurate when the Bessel function argument is large compared to the order. Also Eq. (6) is satisfied only when the eigenvalue is large compared to the order m. Thus it is anticipated that Eq. (5) will be an adequate approximation to Eq. (1) mainly for the higher order radial modes. Implicit to the sine function in Eq. (7) is the assumption that $(1/\xi_{m,\mu})$ approximately defines the location of the principal lobe peak pressure amplitude.

The exact position function for the principal lobe peak pressure, $z^*_{m,\mu}$, can be found by expanding $P'_{m,\mu}$ in a Taylor series about $\alpha_{m,\mu}$, such as:

$$P'_{m,\mu}(z^*_{m,\mu}) = P'_{m,\mu}(\alpha_{m,\mu}) + P''_{m,\mu}(\alpha_{m,\mu})(z^*_{m,\mu} - \alpha_{m,\mu}) + 0.5\, P'''_{m,\mu}(\alpha_{m,\mu})(z^*_{m,\mu} - \alpha_{m,\mu})^2 + \ldots = 0 \qquad (8)$$

Thus, the angular positions of the principal lobe peak pressure can be obtained from

$$(\psi_p)_{m,\mu} = \sin^{-1}\left(\frac{z^*_{m,\mu}}{\pi\eta}\right) \qquad (9)$$

whereas the approximate location is given by (Ref. 7)

$$(\psi_p)_{m,\mu} = \sin^{-1}\left(\frac{1}{\xi_{m,\mu}}\right) \qquad (10)$$

Some difference, therefore, is expected in the predicted position of principal lobes between the exact and approximate equations.

The exact solution of the principal lobe peak pressure can be obtained by substituting the exact position function $z^*_{m,\mu}$ (Eq. (8)) into Eq. (1) yielding

$$(P_p)^2_{m,\mu} = \frac{z^{*2}_{m,\mu} J'^2_m(z^*_{m,\mu})(\pi\eta)^2 \sqrt{1 - (1/\xi_{m,\mu})^2}}{(\alpha^2_{m,\mu} - z^{*2}_{m,\mu})^2\left[1 - (m/\alpha_{m,\mu})^2\right]} \qquad (11)$$

For the approximate approach, the following equation was derived in Ref. 7:

$$(P_p)^2_{m,\mu} \simeq \left(\frac{1}{2}\eta\right) \cot\left[(\psi_p)_{m,\mu}\right] \qquad (12)$$

where $(\psi_p)_{m,\mu}$ is given by Eq. (10).

The difference between the approximate and more exact equations in the number of sidelobes was already mentioned in Ref. 7. In general, the number of sidelobes in an acoustic radiation pattern can be determined from the location of the sidelobe terminal or nodal points. The exact angular locations of the sidelobe terminals can be determined from the following equation:

$$\psi_0 = \sin^{-1}\left(\frac{z_0}{\pi\eta}\right) \qquad (13)$$

where the inverse

$$z_0 = (\pi\eta)\sin\psi_0 \tag{14}$$

is, according to the exact Eq. (1), the solution of the following equation:

$$J'_m(z_0) = 0 \tag{15}$$

The z_0 are recognized as the eigenvalues (see Eq. (4)) excluding the one which produces the principal lobe peak. The total number of the sidelobes then is equal to the total number of the sidelobe nodes, providing that

$$z_0 \leq (\pi\eta) \neq \alpha_{m,\mu} \tag{16}$$

It follows that the exact number of the forward sidelobes, that is, the sidelobes occurring forward of the principal lobe, is identically equal to the radial order number μ

$$s_f = \mu \tag{17}$$

There is no simple analytical expression for the exact number of aft sidelobes. The number, however, increases with the frequency parameter η.

In the approximate approach, the expression for the node location can be written, according to approximate Eq. (5), as follows:

$$\psi_0 = \sin^{-1}\left(\frac{\alpha_{m,\mu} \pm \pi s}{\pi\eta}\right) \tag{18}$$

where s is a positive integer that is also equal to the number of the approximate sidelobes. For the forward sidelobes

$$s_f \simeq \frac{\alpha_{m,\mu}}{\pi} \tag{19}$$

The number of forward sidelobes, therefore, will generally differ for the exact and approximate equations. For the aft sidelobes,

$$s_a \simeq \frac{\pi\eta - \alpha_{m,\mu}}{\pi} \tag{20}$$

and for the total number of sidelobes

$$s \simeq \eta \tag{21}$$

Thus, the total number of the approximate sidelobes, as also noted in Ref. 7, is always constant for the same frequency regardless of mode orders m or μ. The total number of sidelobes obtained from the exact and approximate equations will generally differ.

Multimodal Summation Equations

The total radiated far-field acoustic pressure at any given angular location ψ due to many modes can be expressed by the following summations:

$$P^2(\psi) = \sum_m \sum_\mu \left[P^2_{m,\mu}(\psi)\right] \tag{22}$$

where mean-square acoustic pressure $P^2_{m,\mu}(\psi)$ is given by Eq. (1). Equation (22) will be referred to here as an exact multimodal summation equation. It is assumed that all modes participating in the summation are equally weighted (equal acoustic power per mode). The exact multimodal summation equation includes the contributions from all principal lobes, as well as from all sidelobes at the given directivity angle ψ.

In Ref. 7, the following approximate summation equations were derived:

$$P^2(\psi) \approx 2 \cos \psi \tag{23}$$

for the equal acoustic power per mode case and

$$P^2(\psi) \approx 2 \cos \psi \sin^n \psi \tag{24}$$

for the unequal acoustic power per mode cases where n is an exponent of the acoustic power biasing function

$$\beta_{m,\mu} = (1/\xi_{m,\mu})^n \tag{25}$$

Note that Eq. (23) is a special case of Eq. (24) when $n = 0$. Equations (23) and (24) will be referred to here as the approximate multimodal summation equations. The approximate equations differ from the exact Eq. (22) in that the approximate equations take into consideration only the contributions from the principal lobes at the given angular location ψ. They assume that modes with similar cut-off ratios yield similar principal lobe peak amplitudes, as can be also inferred from the approximate single mode Eq. (5).

COMPARISON OF SINGLE MODE PATTERNS

In this section, several single mode radiation patterns calculated from the exact Eq. (1) are compared to the patterns obtained from the approximate Eq. (5) in order to determine the range of validity of the approximate approach. Three classes of modes are considered: (1) modes with a varying radial order, but with a constant circumferential order and source frequency; (2) modes with a varying circumferential order, but with a constant radial order and frequency parameter; and (3) the last cut-on or propagating modes with a constant circumferential order, but with varying radial order and frequency parameter.

Constant Circumferential Order Modes

Figures 1(a) to (d) show exact and approximate far-field directivity patterns of modes (2, 0, 6.4), (2, 2, 6.4), (2, 3, 6.4), and (2, 5, 6.4), respectively. The figure compares directivity patterns where the total number of sidelobes for the exact and approximate expression are very nearly equal. The designation used here for the modes in the far-field radiation pattern (m, μ, η), differs from the conventional designation of in-duct modes (m,μ), because the directivity patterns in the far field also depend on the source frequency parameter η.

Figure 1(a) shows the differences between principal lobes and the sidelobes of exact (solid lines) and approximate (dash-dash lines) directivity patterns of zero radial order mode (2, 0, 6.4). It is seen that differences exist in the angular spread, angular position of the peak pressure, and the magnitude of peak pressure level of the lobes. The disagreement in the angular locations of the

approximate and exact principal lobes of mode (2, 0, 6.4) is mainly due to the assumption made in formulating the argument of the sine function in the approximate Eq. (5). In Ref. 7 it was assumed that the mode eigenvalue $\alpha_{m,\nu}$ (Eq. (4)) approximately defines the location of the principal lobe peak pressure. However, the exact position function for the principal lobe peak pressure, $z^*_{m,\nu}$, can be found from Eq. (8). On the other hand, Figs. 1(b) to (d) indicate that there is an excellent agreement between the exact and approximate principal lobes of the higher radial order modes (2, 2, 6.4), (2, 3, 6.4), and (2, 5, 6.4), respectively. This is not an unexpected result because the ratio $(m/\alpha_{m,\nu})$ of the constant circumferential order decreases (Eq. (6)) and the argument of the Bessel function increases (Eq. (7)) which for both approximations are in the right direction to improve the accuracy of the approximate Eq. (5).

The agreement between the exact and the approximate sidelobes also improves as radial order increases. It is especially noticeable for the first forward and the first aft sidelobes with respect to the principal lobe. However, in all three higher radial order approximate patterns, an extra pseudo sidelobe appears forward of the principal lobe (near $\psi = 0$), which does not exist in the exact pattern.

Constant Radial Order Modes

Figures 2(a) to (c) show exact (solid lines) and approximate (dash-dash lines) far-field acoustic directivity patterns of modes (3, 0, 6.4), (11, 0, 6.4), and (16, 0, 6.4). The three modes chosen for this section belong to a special class of modes, called zero radial order modes. They represent the limiting case for the use of the approximate single mode Eq. (5), as was already indicated by mode (2, 0, 6.4) discussed in the previous section on the constant circumferential order modes. The zero radial order modes, as seen from Figs. 2(a) to (c), represent the case for which the approximations of Eqs. (6) and (7) will be the least accurate. It should thus be expected that Eq. (5) will also be the least accurate for these modes.

It is seen from Fig. 2 that the differences in the angular spread, location, and peak pressure level between the exact and approximate principal lobes tend to increase as circumferential mode order increases. In particular, one or more pseudo sidelobes appear in the approximate patterns, which do not exist in the exact patterns. The differences in principal lobe peak pressure position could be expected in view of the previous discussion regarding the functions $z^*_{m,\nu}$ and $\alpha_{m,\nu}$. Moreover, the ratio $(m/\alpha_{m,\nu})$ of the zero radial order modes increases as the circumferential mode order increases.

The accuracy of approximate Eq. (5) can be improved by substituting the position function $z^*_{m,\nu}$ for mode eigenvalue $\alpha_{m,\nu}$ in the sine function. The results are shown in Figs. 2(a) to (c) by solid-dash-solid lines. For the worst case shown here (Fig. 2(c)), even though the detailed structure of the lobe patterns is different for the exact and the approximate calculations, the gross behavior of the principal lobe is described by the approximate equation. It was pointed out in Ref. 7 that for multimodal radiation patterns, errors of the kind shown in Fig. 2(c) for a relatively few modes (mainly zero order modes) will not be significant. This will be seen to be true in a later section of this paper.

Last Propagating or Cut-On Modes

Figures 3(a) to (c) compare exact and approximate directivity patterns of modes (16, 0, 6.4), (16, 2, 9.5), and (16, 5, 12.7), respectively. They represent a class of modes, which are the last propagating or cut-on modes of a number of possible propagating or cut-on modes. The last cut-on mode in a set of several propagating modes having the same circumferential order m may be defined as the mode for which

$$\alpha_{m,\mu} = (\alpha_{mn}) \quad \alpha_{m,\mu+1} \tag{26}$$

The last cut-on modes are of particular interest to the duct suppressor designer because these modes radiate mainly to the engine sideline and they can be attenuated easier than other modes. They also have certain properties not possessed by other modes. For example, the last cut-on modes have a relatively low cut-off ratio $\xi_{m,\mu}$ approaching unity or the mode actual cut-off. For modes (16, 0, 6.4), (16, 2, 9.5) and (16, 5, 12.7), the cut-off ratios are 1.11, 1.10, and 1.05, respectively. Figure 3 shows that as a consequence of relatively low cut-off ratios, the principal lobes of exact and approximate patterns have the following three features in common. They (1) peak near 90°-sideline; (2) are incomplete; and (3) are the last lobes in the pattern.

The last cut-on modes, considered in this section, were obtained by keeping the circumferential mode order m constant and varying the source frequency parameter η. This resulted in the modal structures with increased radial mode order μ. Thus it is seen from Fig. 3 that the effect of increased frequency parameter η on exact and approximate directivity patterns is similar to that already discussed in the section on the constant circumferential order modes, that is, the differences tend to decrease as the frequency parameter and radial order increase. As previously pointed out, the error in the approximate Eq. (5) regarding the principal lobes will not significantly affect the multimodal radiation calculations.

ASSUMPTIONS ABOUT PRINCIPAL LOBES

In deriving the approximate multimodal summation equations in Ref. 7, such as Eqs. (23) and (24) introduced here, several assumptions were made about the role of the principal lobes. For example, it was postulated that the mode eigenvalue $\alpha_{m,\mu}$ or more precisely the reciprocal of the mode cut-off ratio $\xi_{m,\mu}$ approximately defines the angular location of the principal lobe peak pressure (e.g., Eq. (10)).

Comparison of the approximate and exact patterns presented previously in Figs. 1 to 3 indicated that this assumption gave a very good agreement for all higher radial order modes. But it was also shown that for lower and especially for zero radial order modes the approximate location of the principal lobe peak pressure differed from the exact location. The reason for the difference was because the exact location of the principal lobe peak pressure is determined by the position function $z^*_{m,\mu}$ given by Eq. (8) rather than by the mode eigenvalue $\alpha_{m,\mu}$ used in the approximate approach (e.g., Eq. (4)).

The values of principal lobe position function $z^*_{m,\mu}$ and mode eigenvalues $\alpha_{m,\mu}$ are compared in Fig. 4 which shows that the values of function $z^*_{m,\mu}$ consistently exceed the eigenvalues $\alpha_{m,\mu}$ for all zero radial order modes. How-

ever, for the modes with radial orders greater than zero, the difference between the two values becomes smaller as radial mode order increases.

Figure 5 shows the angular variation of the approximate and exact relative directivity level of the principal lobe peak pressure. For the given frequency parameter η of 6.4, fifty-two cut-on modes are involved (omitting modes with a circumferential order equal to zero). The dash-dash curve represents the loci of the approximate principal lobe peak pressure level as calculated from Eq. (12) with the directivity angle defined by Eq. (10). The symbols show the exact relative directivity level of the principal lobe peak pressure (Eq. (11)) with the directivity angle defined by Eq. (9). The exact levels contrary to the approximate levels do not follow a single curve. Instead, it appears that they tend to form clusterlike structures falling in a seemingly unorganized fashion on or below the approximate curve (Eq. (12)) within about 2 dB. A closer look at the discrete points, however, indicates that they are quite organized. In general, the lowest point at any angle ψ represents the zero radial order mode. The point above is for the next higher radial order mode, and so on. The approximate curve generally cuts through the points representing the modes having the highest radial order. An exception occurs near the 90° angle where the approximate curve falls below the exact points. At 90°, as seen from Eq. (12), the approximate principal lobe peak pressure is equal to zero. As seen from Fig. 5, the exact principal lobe peak pressure, obtained from Eq. (11), has a finite value at 90° greater than zero. The three groups of points encircled at about 15°, 45°, and 70° will be subsequently discussed.

As stated in Ref. 7, one of the implications of approximate single mode Eq. (5) is that all modes with approximately the same cut-off ratio will have approximately the same radiation pattern. It follows then that all modes with approximately the same cut-off ratio $\xi_{m,\mu}$ also will have approximately the same principal lobe peak pressure level and angular position (e.g., Eq. (10)). Equation (10) also shows that as the cut-off ratio approaches unity, the approximate angular position of principal lobe peak pressure approaches 90°. The mode cut-off ratio diagram shown in Fig. 6 displays the 52 modes used in the previous figure as a function of the cut-off ratio. It is seen that the mode cut-off ratio density increases considerably as the cut-off ratio of the modes approaches unity. It might be expected then that the maximum density of the principal lobe peak pressure level would occur near the 90°-sideline. However, Fig. 5 indicates that the region between about 15° and 75° is the most densely populated region. On the other hand, the regions near the axis and 90°-sideline have only 2 and 3 principal lobe peaks, respectively. Moreover, in the region near the 90°-sideline, the portion between modes (2, 5, 6.4) and (7, 3, 6.4), approximately 10° wide, is completely void of any principal lobe peaks. The dispersion in angular position of the high density of the modes with cut-off ratios near unity results from the nonlinear relation between cut-off ratio and angular position (Eq. (10)). The cut-off ratio abscissa, also shown in Fig. 5, illustrates this nonlinear relation.

The three previously identified groups of principal lobes at about 15°, 45°, and 70° (Fig. 5) are further studied in Fig. 7. The figure shows the relative directivity level of individual principal lobes, overall levels, and multimodal summation levels as obtained from the exact equation. Similarity of individual principal lobe contours, peak levels, and angular locations within each group of modes is apparent and tends to substantiate the assumption of similarity made in developing the approximate summation equations. In addition, Fig. 7 shows an ex-

cellent agreement between exact (Eq. (22)) and approximate (Eq. (23)) multimodal summation equations. There is also a relatively good agreement between the level of the multimodal summations and the overall lobe peak level for the first cluster. For the second and the third clusters, the overall lobe peak levels are below the multimodal summation level by about 3 and 7 dB, respectively. The decibel shortage indicates that more modes than contained within the mode groups in Fig. 7 contribute to the total summation.

MULTIMODAL SUMMATION

Figures 8(a) to (c) compare the angular distribution of relative directivity level of exact (Eq. (22)) and approximate (Eqs. (23) and (24)) multimodal summations. Altogether, three far-field directivity models are considered: (1) equal acoustic power per mode, $n = 0$; (2) unequal acoustic power per mode, $n = 1$; and (3) unequal acoustic power per mode, $n = 3$, where n is the exponent of the acoustic power biasing function $\beta_{m,\mu}$ (Eq. (11)). In addition, points representing single mode exact principal lobe peak pressures (Eq. (11)) and loci of approximate principal lobe peak pressure (Eq. (12)) are also shown in the figures.

It is seen from the figures that for all three directivity models considered, there is, in general, excellent agreement between approximate and exact summations. The results indicate that the errors in the lobe approximations are not significant in the total summation for a distribution of modes, regardless of the directivity model. The single mode errors in the principal lobe peak pressures are indicated in Fig. 8 by the deviation of the single mode symbols from the approximate top curve. It is seen that the largest deviation, as discussed previously (e.g., Fig. 5), are exhibited by the zero and low radial order modes. Thus, it also appears that the final result may be mainly controlled by the distribution of the higher radial order modes.

MODAL PARTICIPATION

The excellent agreement between exact and approximate multimodal summations found in the previous section is partly explained by the higher radial order modes exerting the controlling effect on the final result of the exact summation. This explanation is based on the previous observations that the principal lobe peak level loci, represented by a single curve in the approximate approach, is the upper limit approached by the exact principal lobe peak directivity levels of the higher radial order modes. Consequently, this raises the questions about how significant then is the contribution by the lower radial order modes (zero order in particular) to the final result and whether it is necessary to account for all the participating modes to achieve similar far-field directivity patterns.

A modal participation in a multimodal summation ($n = 1$) is illustrated in Fig. 9. Altogether, a total of 78 propagating or cut-on modes are involved for the given source frequency parameter η of 7.8. The modes have circumferential mode order m ranging from 1 to 22 with anywhere from 1 to 8 radial orders participating in each circumferential order. In Fig. 9(a), the total modal distribution for each circumferential order is shown at 7 discrete angles from about 12.5° to 80.5°. The solid lines connect the contributions at each angle of all the radial order modes associated with each circumferential order. At each angle, all circumferential orders are participating, but the contribution by some orders is relatively small and can be neglected. The angular levels singled out by

square symbols indicate the last circumferential order that is still making a relatively significant contribution (0.5 dB) to the overall level at that angle. For example, at the angle of 12.5° there are 5 circumferential orders (containing 34 radial order modes) which make significant contributions at this directivity angle. The contribution of the remaining 17 circumferential orders at angle 12.5° is negligible. As directivity angle increases, more circumferential orders are participating with significant contributions.

The lower circumferential orders are contributing more than the higher circumferential orders because they have more cut-on radial order modes. Not all radial order modes, however, contribute equally. An example, showing radial order mode contributions, is illustrated in Fig. 9(b) for the modes having the circumferential order $m = 1$. The contribution of each of the total of 8 possible cut-on radial order modes is shown at discrete angles. The figure shows that at the majority of the discrete directivity angles, a single radial order mode having its principal lobe peak at or very close to these angles establishes the overall level. Furthermore, it is seen that the overall level is established by modes having radial order greater than zero. Figure 9(b) also shows that the overall level of the $m = 1$ modes has a directivity that differs from that of the total summation from all circumferential orders. It indicates that more than a single circumferential order must be considered at each angle to achieve a directivity pattern similar to the total summation directivity pattern.

Figure 9(c) compares the exact (Eq. (8)) and approximate (Eq. (10)) multimodal summation results for a directivity representative of experimental data. The data are for the blade passing frequency tone and were obtained from a full scale high bypass research fan tested at 90 percent fan speed in a static outdoor acoustic test facility at NASA Lewis Research Center (Ref. 8). A good agreement is indicated at all seven directivity angles by using an acoustic power biasing exponent n equal to 7.8.

SUMMARY OF RESULTS

In this paper, several single mode and multimodal radiation patterns calculated from exact equations were compared to the patterns obtained from Rice's approximate equations to determine the range of validity of the approximate approach. For the single mode cases, the gross behavior of the principal lobes was described by the approximate equation. For higher radial order modes there was, as expected, an excellent agreement between the exact and approximate contours, peak levels, and angular positions of all the principal lobes considered in this paper. The approximate single mode equations were found to be the least accurate for the zero radial order modes. Some agreement between the exact and approximate sidelobes was observed although the approximate equation was not intended to simulate the sidelobes.

Several individual groups of closely spaced principal lobes were checked for the similarity characteristics assumed in formulating the approximate summation equations. It was shown that modes with similar cut-off ratios have similar principal lobe peak levels at approximately the same directivity angles as assumed.

A comparison of exact and approximate multimodal summation equations showed an excellent agreement between approximate and exact summations. Examples of

three different distributions of modal acoustic power indicated that sidelobes have a negligible effect on the multimodal directivity level, and the summation is mainly controlled by the principal lobes of higher radial order modes.

The significance of zero and lower radial order modes to the final result and the number of modes needed to achieve similar far-field directivity patterns was examined by tracing the contributions of the sets of radial order modes having the same circumferential order and by tracing, on a selective basis, the contributions of single radial order modes in a constant circumferential order set. The result demonstrated that the main contributions appeared to come from higher radial order modes. Good agreement was also achieved between exact and approximate summations for a directivity typical of experimental data.

REFERENCES

1. G. F. Pickett, T. G. Sofrin, and R. W. Wells, "Method of Fan Sound Mode Structure Determination," NASA CR-135293 (August 1977).

2. P. M. Morse, Vibration and Sound (McGraw-Hill, New York, 1948) 2nd. ed.

3. J. M. Tyler and T. G. Sofrin, "Axial Flow Compressor Noise Studies," SAE Trans. 70, 309-332 (1962).

4. D. L. Lansing, J. A. Drischler, and C. G. Pusey, "Radiation of Sound from an Unflanged Circular Duct with Flow," paper presented at the 79th Meeting of the Acoustical Society of America, Atlantic City, NJ, April 21-24, 1970.

5. G. F. Homicz and J. A. Lordi, "A Note on the Radiative Directivity Patterns of Duct Acoustic Modes," J. Sound Vib. 43 (3), 283-290 (1975).

6. A. V. Saule, "Modal Structure Inferred from Static Far-Field Noise Directivity," AIAA Paper No. 76-574 (July 1976); also NASA TM X-71709 (1976)

7. E. J. Rice, "Multimodal Far-Field Acoustic Radiation Pattern - An Approximate Equation," AIAA Paper No. 77-1281 (October 1977); also NASA TM 73721 (1977).

8. A. V. Saule, "Some Observations About the Components of Transonic Fan Noise from Narrow-Band Spectral Analysis," NASA TN D-7788 (1974).

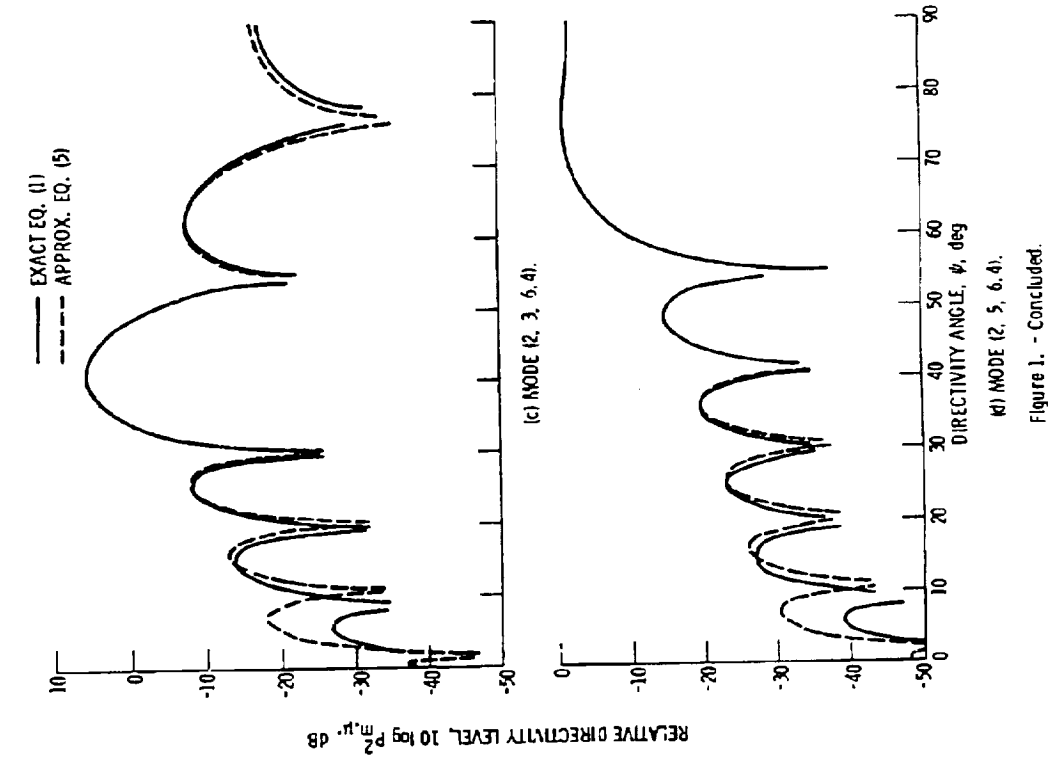

Figure 1. - Concluded.

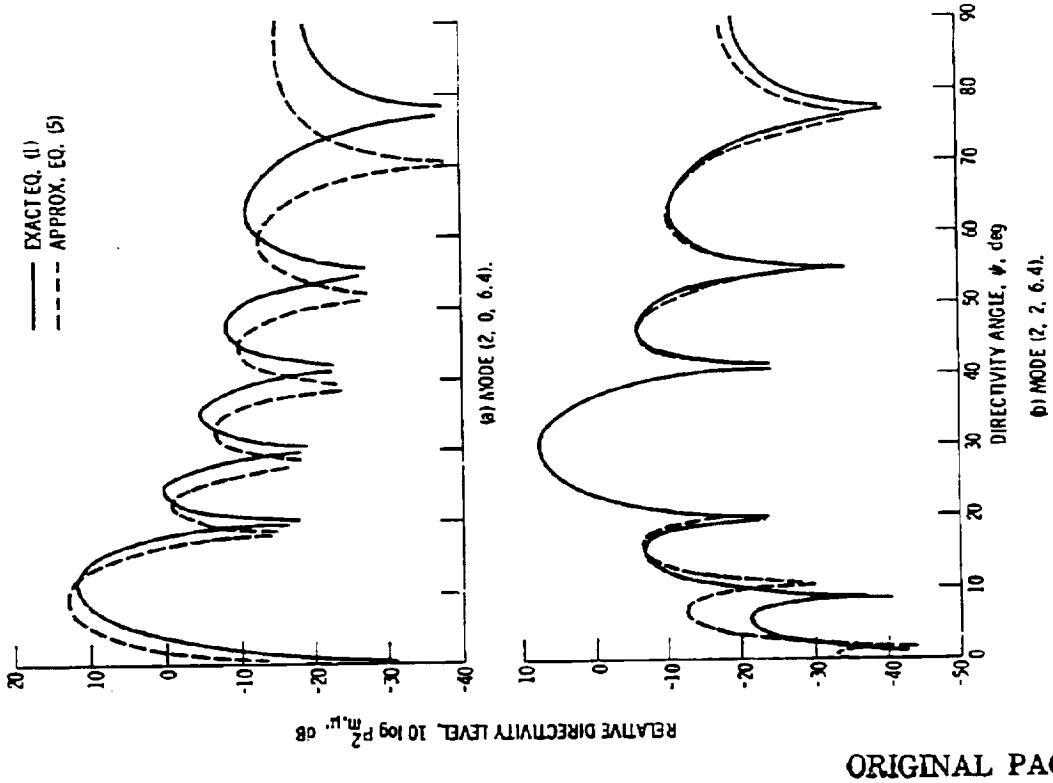

Figure 1. - Comparison of exact and approximate directivity patterns produced by modes with equal circumferential order.

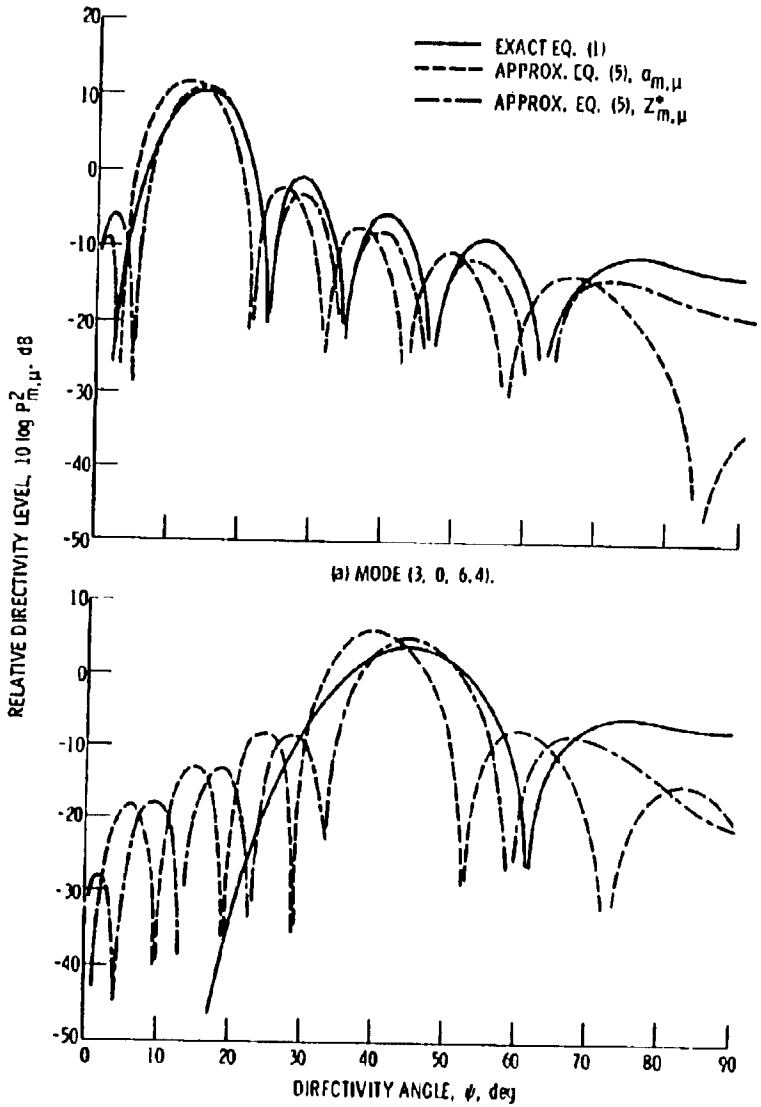

(a) MODE (3, 0, 6,4).

(b) MODE (11, 0, 6,4).

Figure 2. - Comparison of exact and approximate directivity patterns produced by modes with equal radial order.

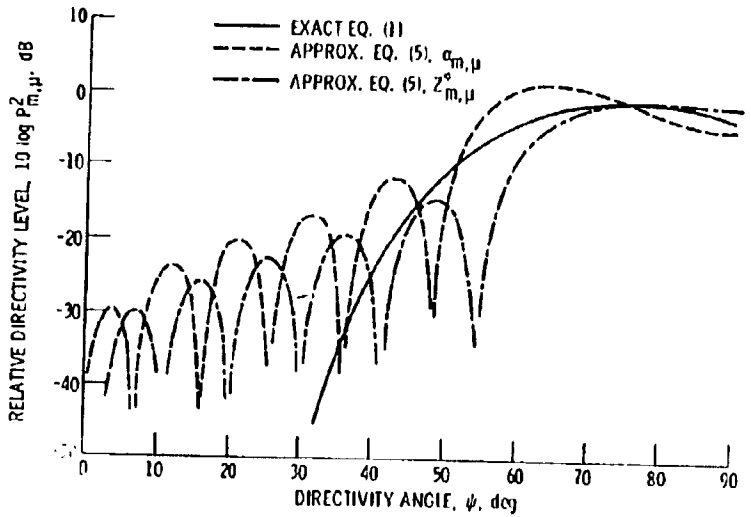

(c) MODE (16, 0, 6.4).

Figure 2. - Concluded.

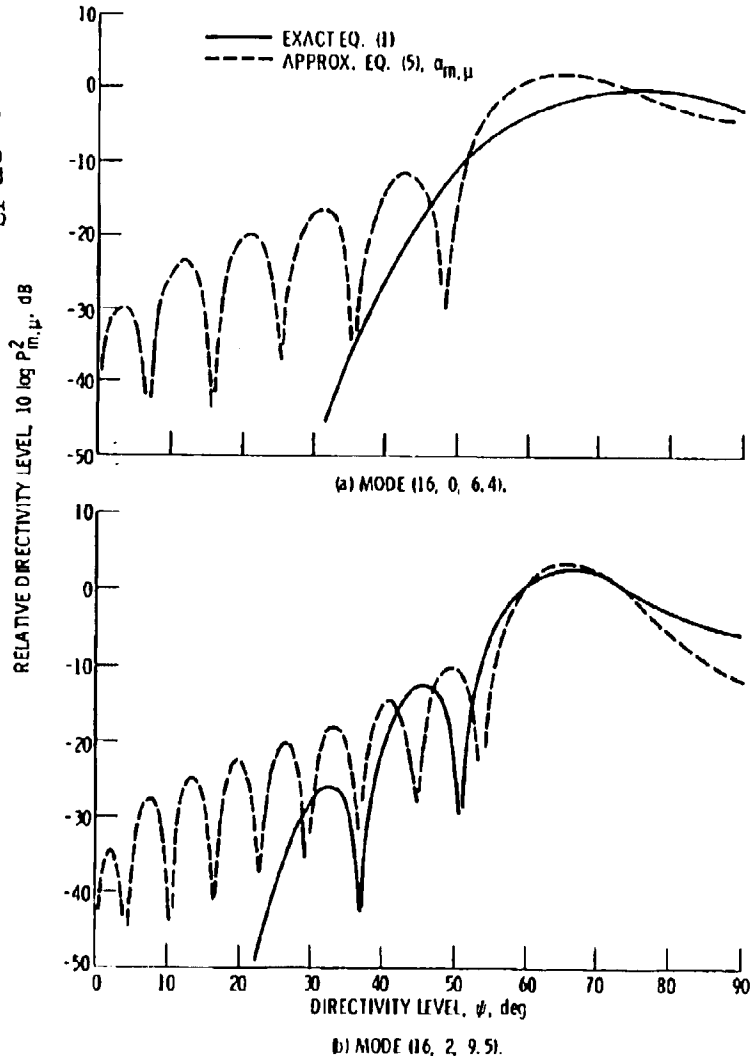

(a) MODE (16, 0, 6.4).

(b) MODE (16, 2, 9.5).

Figure 3. - Comparison of exact and approximate directivity patterns produced by fast propagating or cut-on modes.

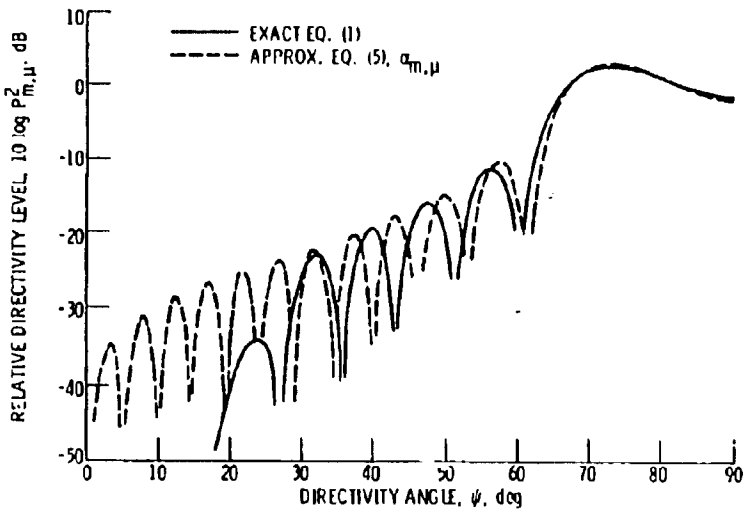

(c) MODE (16, 5, 12.7).

Figure 3. - Concluded.

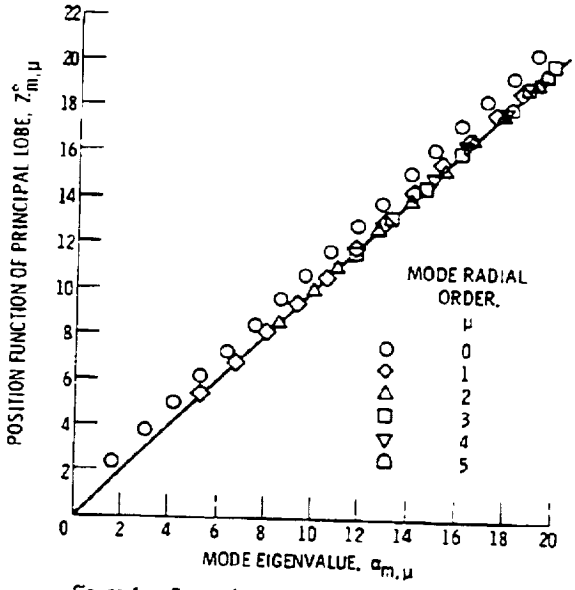

Figure 4. - Comparison of mode eigenvalues and position functions of principal lobes, $\eta = 6.4$.

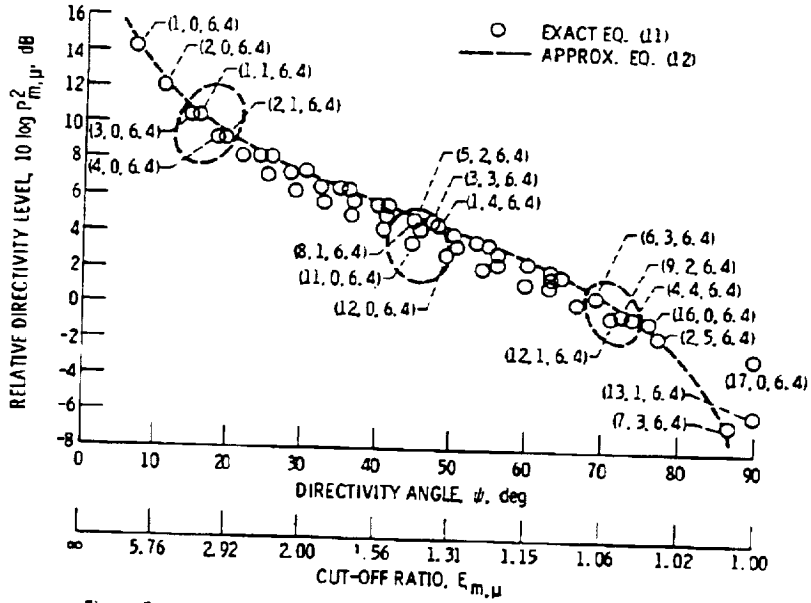

Figure 5. - Angular variation of approximate and exact relative directivity level of principal lobe peak pressure, $\eta = 6.4$.

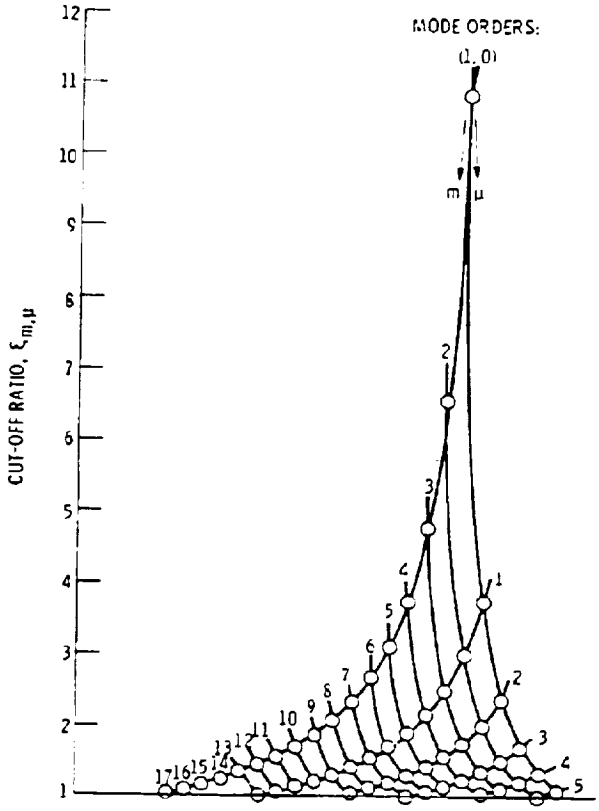

Figure 6. - Diagram of mode cut-off ratios, $\eta = 6.4$.

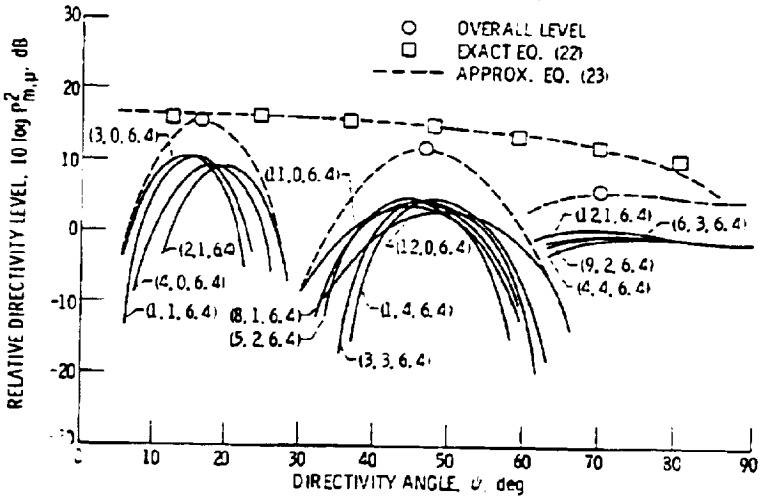

Figure 7. - Comparison of principal lobe cluster overall and multimodal summation levels, $\eta = 6.4$.

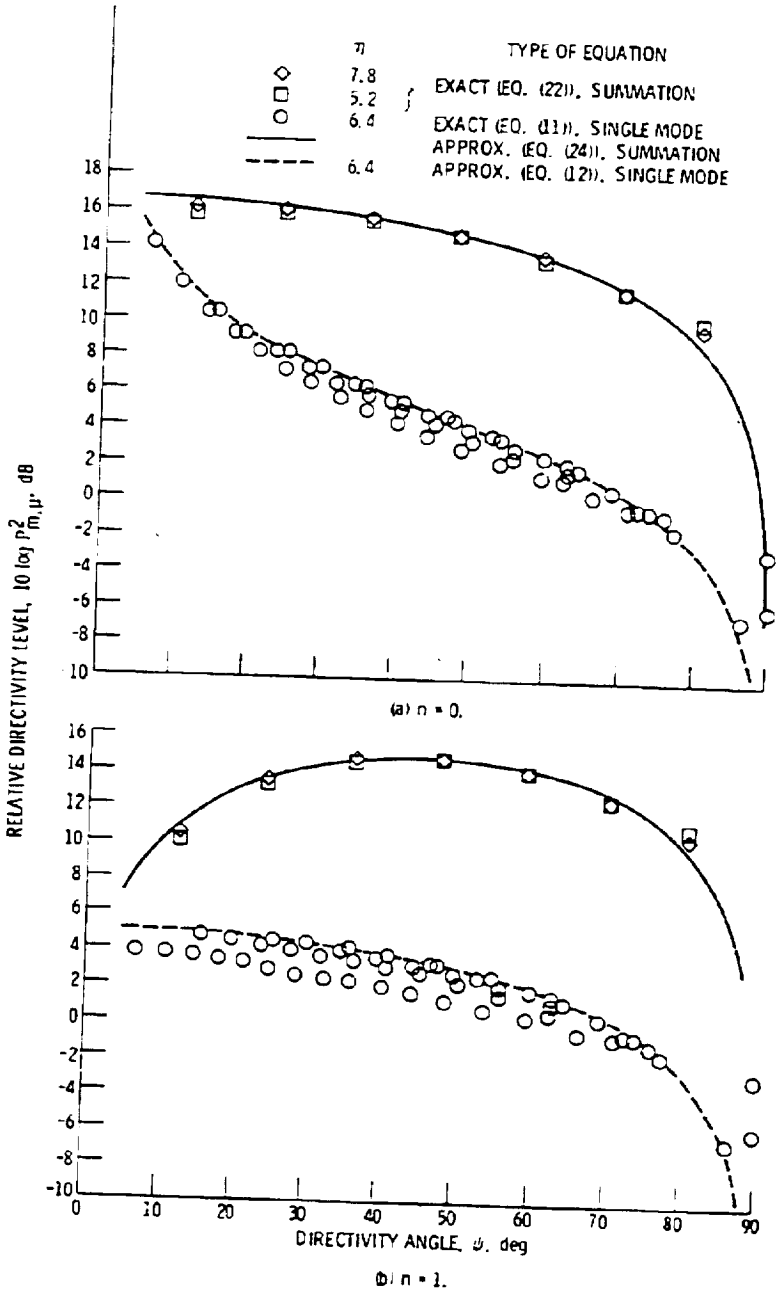

Figure 8. - Comparison of approximate and exact multimodal summation levels.

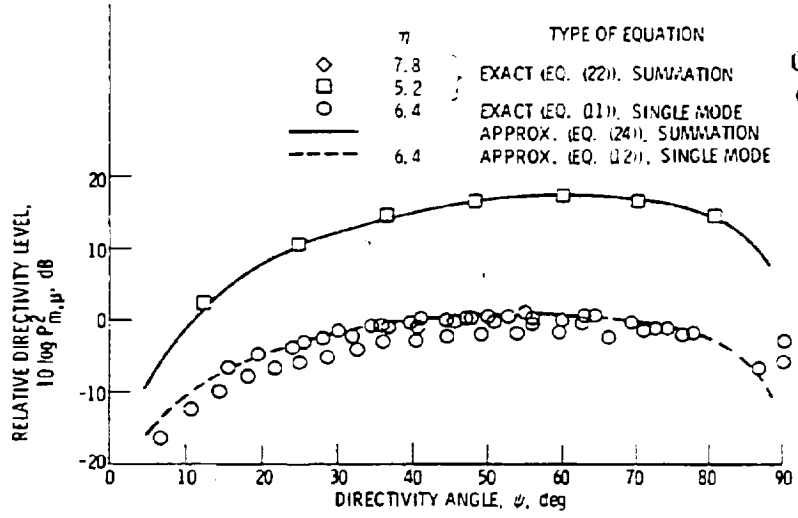

(c) n = 3.

Figure 8. - Concluded.

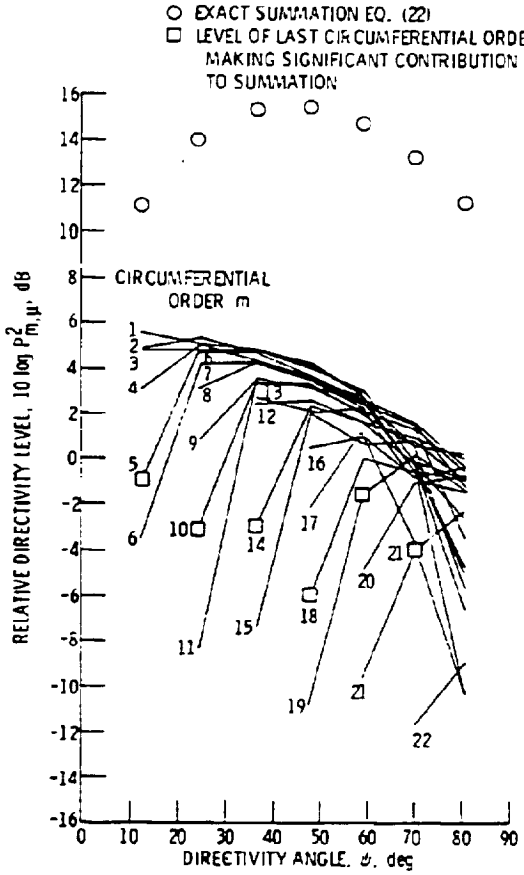

(a) SETS OF RADIAL ORDER MODES OF CIRCUMFERENTIAL ORDER m.

Figure 9. - Modal participation in multimodal directivity, η = 7.8, η = 1.

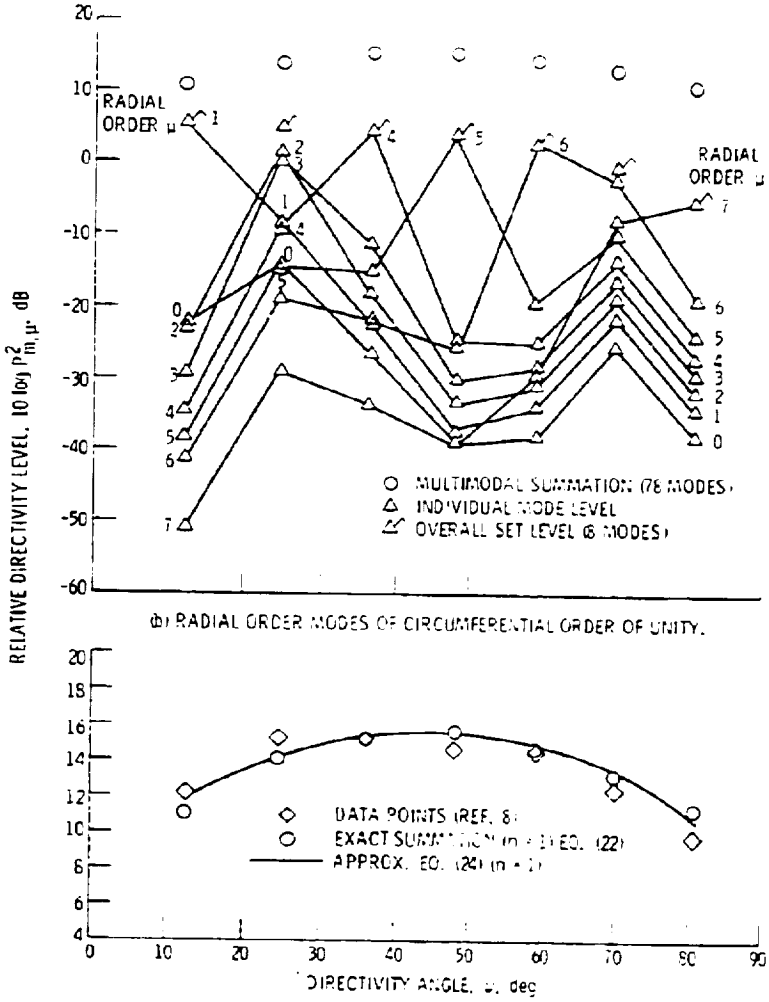

(b) RADIAL ORDER MODES OF CIRCUMFERENTIAL ORDER OF UNITY.

(c) COMPARISON OF SUMMATIONS WITH DATA.

Figure 9. - Concluded.